The influence of preparation pressure on the electrochemical performance of semiconductor-ionic membrane fuel cells (SIMFC)

Yi Jiang[1] · Hui Huang[1] · Mengqiu Wang[1] · Weiwei Zhang[1] · Baoyuan Wang[1]

Abstract

Recently, semiconductor-ionic membrane fuel cells (SIMFC) has been widely reported due to its excellent power output. In general, the SIMFCs were fabricated by dry pressing method without high-temperature sintering, thus the preparation pressure is bound to affect the microstructure of electrolyte and electrode and further determine the cell performance. To detect the influence of preparation pressure, SIMFC based on La and Pr co-doped CeO_2–$Ni_{0.8}Co_{0.15}Al_{0.05}LiO_{2-\delta}$ electrolyte was fabricated under different preparation pressure. The evolution of cell microstructure and cell performance with preparation pressure were systematically characterized to obtain the optimal pressure. The characterizations revealed that the increase of preparation pressure gave rise to the enhancement of electrolyte density and the decrease of the electrode porosity, and further brought about the improvement of the gas tightness of the electrolyte membrane and the decrease of three reaction phase area of electrode; the two factors gave the opposite effect to the cell performance and reached a balance at certain preparation pressure. Therefore, the performance of the assembled cell initially increases and then decreases with the increase of preparation pressure, an optimal performance, i.e., a power maximum of 833 mW cm^{-2} and open circuit voltage of 1 V, was obtained at 550 °C when the preparation pressure is 10 MPa.

1 Introduction

The massive application of fossil fuels has greatly damaged our environment and energetically spurred the development of clean energy. Hydrogen energy as a promising clean energy sources has attracted widespread attention at present [1, 2]. Various devices were exploited to make use of hydrogen. Among them, solid oxide fuel cell (SOFC) as an electrochemical device can directly convert the chemical energy in hydrogen to electrical energy. Recently, SOFC has become a research hotpot due to its excellent efficiency, fuel diversity, promising stability and environmental friendship [3–6]. Besides, SOFC presented great potential in the commercial market during its rapid development [7, 8]. The conventional SOFC usually consists of three components including cathode, anode and electrolyte membrane [9, 10]. However, high operating temperature (above 800 °C)

is indispensable to fulfill the desired ion conductivity of electrolyte and the excellent catalytic activity of electrode. Simultaneously, the high operational temperature causes lots of thorny problems and serious restriction to the commercialization of SOFCs [11]. Recently, the semiconductor-ionic conductor membrane fuel cell (SIMFC) fabricated from various semiconductor-ion conductor materials (SIMs) have been widely demonstrated due to their promising performance at intermediate–low temperature. For example, Deng et al. reported that the SIMFC based on $Sr_2Fe_{1.5}Mo_{0.5}O_{6-\delta}$ (SFM)–$Ce_{0.8}Sm_{0.2}O_{2-\delta}$(SDC) electrolyte deserved the peak power output of 841 mW cm^{-2} at 550 °C [12]. Xia et al. fabricated a SIMFC from ZnO–$La_{0.33}Ce_{0.62}Pr_{0.05}O_{1.6}$ (LCP) SIM electrolyte, and such device presented high maximum power density (P_{max}) of 864 mW cm^{-2} at 550 °C [13]. Zhu et al. used the $LiNi_{0.1}Fe_{0.90}O_{2-\delta}$ (LNF)–SDC SIMs electrolyte to assemble SIMFC, and the peak power density reached up to 760 mW cm^{-2} at 550 °C [14].

In these SIMFCs, the SIMs were commonly applied as electrolyte membrane and two $Ni_{0.8}Co_{0.15}Al_{0.05}LiO_{2-\delta}$ (NCAL) layers were, respectively, utilized as anode and cathode to assemble symmetrical cell. The high electrochemical performance of SIMFC at intermediate–low temperature originated from the super-ion conductivity of SIMs

✉ Baoyuan Wang
  baoyuanw@163.com

1   Key Laboratory of Ferro &Piezoelectric Materials
    and Devices, Faculty of Physics and Electronic
    Science, Hubei University, Wuhan 430062, Hubei,
    People's Republic of China

electrolyte and the excellent catalytic activity of $(H^+/O^{2-}/e^-)$ triple-conductor NCAL electrode. Besides, during cell operating, a Schottky junction was in situ formed between the reduced NCAL anode and SIM electrolyte, and the accompanying built-in field can prevent the electron from passing through the cell interior and simultaneously accelerate the ion conducting; therefore, the shorting circuit problem have been successfully solved and the cell performance has been boosted.

As previous reports presented, the fabrication procedure for SIMFC has eliminated the high-temperature sintering in comparison with conventional fuel cell, and thus the microstructure of electrodes and electrolyte were determined by the preparation pressure. However, electrode and electrolyte have adverse expectance on microstructure to improve the cell performance. For example, the NCAL electrodes were expected to have perfect porosity, which is in favor of transferring gaseous fuel and air to extend the three-phase boundaries (TPB) and accelerate the reaction rate. However, a promising density is required for electrolyte membrane; the dense electrolyte membrane can provide desired gas tightness and prevent the fuel from contacting with air [15]. Thus, it exhibited great significance to optimize preparation pressure in cell preparation process.

In this study, LCP–NCAL SIMFC was used as electrolyte membrane to assemble SIMFC under different pressure. We mainly focused on the effect of pressure on the microstructure and electrochemical performance of SIMFC to obtain the optimal preparation pressure and the underlying effect mechanism.

2 Experimental

2.1 Materials

The precursor material of LCP was commercial rare-earth carbonates, which was directly purchased from Baotou rare-earth company. As the composition table from rare-earth company manifested, the rare-earth precursor consisted of $La_2(CO_3)_3$ (24.9 wt%), $Ce_2(CO_3)_3$ (74.7 wt%), and $Pr_2(CO_3)_3$ (0.4 wt%), which were suffered from a sintering at 800 °C for 2 h. After complete grinding, a homogeneous powder in red was gained; the resultants were denoted as $La_{0.33}Ce_{0.62}Pr_{0.05}O_{1.6}$ (LCP). NCAL as a commercial product was directly purchased from Tianjin Baomo Joint Hi-Tech venture, China, and then mechanically mixed with LCP in 1:1 weight ratio through complete grinding to get an uniform LCP–NCAL SIM. Although there is no special procedure for the preparation of LCP–NCAL SIM, the experimental procedure, including the full grinding to LCP–NCAL SIM as well as the hydraulic pressure and pre-heating to device, ensured the complete contact and interface formation between the

two-phase materials took place. Moreover, a proper ratio of PVDF (5 wt%) was added as binder due to its viscidity, which can form reticular conglutination to improve the moldability of LCP–NCAL SIM [16–19]. In addition, previous work revealed that a proper ratio of PVDF binder in cells can be completely removed by heat-treatment; the remaining pores can enlarge TPB of the fuel cells, and further leads to a great enhancement on performance of devices [20].

2.2 Fabricating fuel cell and testing performance

With regard to the cell preparation process, firstly the NCAL commercial powder was uniformly blended with glycerol to form a paste, which was painted on Ni-foam and dried at 300 °C to obtain the Ni–NCAL pieces. The LCP–NCAL SIM was sandwiched by two pieces of Ni–NCAL layers to assemble a configuration of Ni–NCAL/NCAL–LCP/Ni–NCAL, which was pressed uniaxially under a series of pressures, such as 6 MPa, 8 MPa, 10 MPa, 12 MPa, to fabricate disc-type cells, wherein the two Ni–NCAL layers, respectively, worked as cathode and anode due to its excellent catalysis activity and $(H^+/O^{2-}/e^-)$ triple conductivity. The LCP–NCAL SIM functioned as electrolyte membrane. In addition, foam Ni as metal support can improve mechanical strength of the assembled cell, and the porous foam structure is conducive to transmit oxygen and hydrogen and further increases the triple-phase boundary (TPB) to speed up chemical reaction in SOFCs. Furthermore, the high conductivity of Ni will decrease the impendence of cells as it was applied as collected electrode [21]. The diameter of the resulting cells is 13 mm and the thickness is 2.2 mm. These cells before testing were sintered in oven at 550 °C for 2 h to burn out the PVDF.

The cell performance was characterized by a computerized instrument (ITECH8511, ITECH Electrical Co., Ltd.). Hydrogen and atmosphere air were continually supplied as fuel and oxidant during the cell operating; the hydrogen flow rate was adjusted from 75 to 200 ml min^{-1}, and the flow rate of air was fixed at 150 ml min^{-1}.

2.3 Characterization

The electrochemical impedance spectra (EIS) were obtained by an electrochemical workstation (Gamry reference 3000). The frequency of the AC signal was in the range of $0.1–10^5$ Hz and the amplitude was 10 mV; the raw data were fitted by ZSimDemo software.

A Bruker D8 X-ray diffractometer (XRD, Bruker Corporation, Germany) was used to characterize the crystal structure of samples using Cu Ka radiation ($\lambda = 0.154060$ nm) as the source. The morphology feature of samples was detected by field emission scanning electron microscope (FESEM,
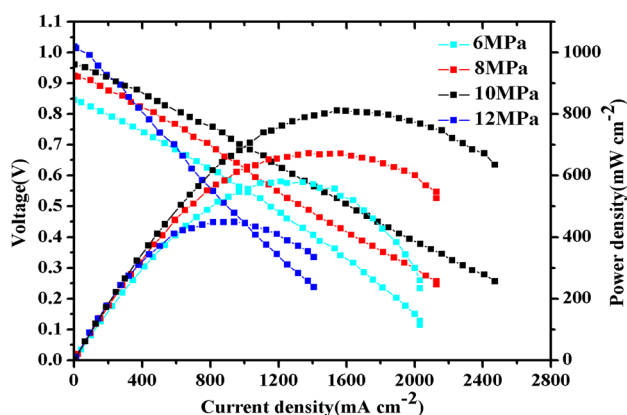
Fig. 1 **a** *I–V* and *I–P* characteristics of LCP–NCAL SIMFC pressed under different loadings; the flow rates of hydrogen and air was fixed at 150 ml min^{-1} during the operating

JSM7100F, Japan) equipped with an Oxford energy-dispersive spectrometer (EDS).

3 Results and discussion

3.1 The performance of SOFCs

Figure 1a depicts the characteristic current density–voltage (*I–V*) and current density–power (*I–P*) curves of LCP–NCAL SIMFC obtained under different pressures. It can be seen that the OCV and P_{max} preliminarily improved as the preparation pressure increased from 6 to 10 MPa and then decrease as the pressure further increased to 12 MPa. The optimal performance, i.e., OCV of 1.01 V and P_{max} of 811 mW cm^{-2}, was received for the LCP–NCAL SIMFC pressed under 10 MPa loading. It is well known that if the electrolyte membrane is insufficiently dense, the gas leakage occurs in the fuel cell, which can bring about the decrease of oxygen partial pressure to further deteriorate the OCV and power output according to Nernst equation. Moreover, gas leakage can also result in the contact between oxygen and hydrogen to cause fierce burning and thereby increases the local temperature, which further gives rise to the decease of OCV [15]. The above analysis demonstrated that the electrolyte density enhanced with the increase of preparation pressure, and it is beneficial to the electrochemical performance enhancement of SIMFC. On the other hand, the porous electrodes are the basic requirement for fuel cell to extend the three-phase boundaries (TPB). As the preparation pressure improved, the porosity of electrodes was deteriorated and the TPB was reduced, which is detrimental for cell performance. In conclusion, the preparation pressure can influence the cell microstructure from two aspects. More specifically, the density of electrolyte was enhanced, and the

porosity of electrode was reduced as the preparation pressure improved; the two changes on microstructure have the adverse influence on cell performance and reach a balance when the preparation pressure was 10 MPa [22–25].

3.2 EIS analysis

To detect the influence of preparation pressure on charge conduction, the EIS measurements were conducted on LCP–NCAL SIMFCs, which were prepared under different pressures. Figure 2a presents the Nyquist curves obtained in H$_2$/air atmosphere at 550 °C, and the experimental result was fitted by equivalent circuit model of $R_0(R_1Q_1)(R_2Q_2)$. As shown in Fig. 2a, the simulation result is well agreed with the experimental date, indicating the availability of equivalent circuit mode. Table 1 listed the detailed parameters obtained by simulation. In the equivalent circuit mode, R_0 is generally assigned to ohmic resistance, and the value of it which equaled to the first intersection of real axis at high frequency [26] dominate the ion conducting, the electron migration and the contact resistance between the cell components [27]. It can be found in Table 1 that R_0 initially decreased from 0.1904 to 0.0472 Ω cm^2 as the preparation pressure increased from 6 to 10 MPa, and then improved to 0.0548 Ω cm^2 when the preparation pressure reached up to 12 MPa. Obviously, the cell pressed at 10 MPa represented the lowest ohmic resistance, which contributed to the optimal cell performance. The lowest Ro maybe came from the superior microstructure of cell as well as the optimal contact between cell components. Moreover, it is noting that all the ohmic resistance (R_0) from LCP–NCAL SIMFCs are much lower than that of cell based on pure LCP electrolyte [28]; the high electrical conductivity of NCAL component in electrolyte membrane contributed to the low ohmic resistance. In
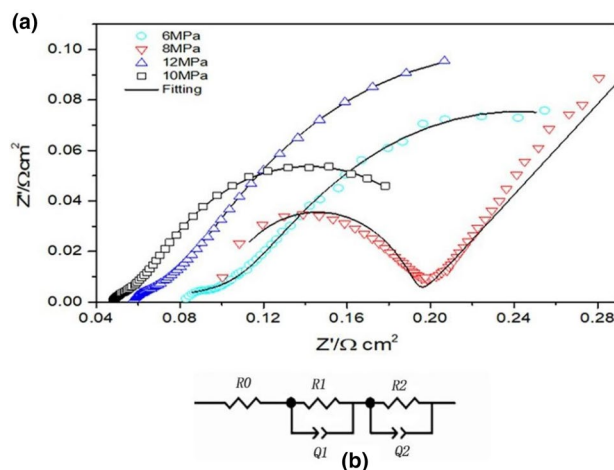

Fig. 2 **a** EIS of LCP–NCAL fuel cells pressed under various pressures and **b** the equivalent circuit model for simulation

Table 1 The fitting results of EIS

Pressure (MPa)	R_0	R_1	Q_1	n_1	C_1	R_2	Q_2	n_2	C_2
6	0.1904	0.2295	5.587	0.8000	5.945	0.3283	3.107	0.7191	3.131
8	0.0551	0.0256	3.684	0.4636	0.240	0.2055	4.662	0.7594	4.599
10	0.0472	0.0187	2.936	0.4976	0.156	0.155	3.859	0.7629	3.289
12	0.0548	0.0468	5.8	0.3415	0.469	0.2874	5.694	0.7375	6.785

addition, the arc in different frequency range can be identified as different electrochemical process according to the characteristic capacitance, which was deduced by the classic formula:

$$C_i = \frac{\left(R_i * Q_i\right)^{1/n_i}}{R_i} \qquad (1)$$

where Q is a non-ideal capacitor and named as the constant phase element. R_i is the resistance corresponded to different arc. Finally, the parameter n denoted the similarity of Q to an ideal capacitor [26, 29]. Meanwhile, the arc at high frequency corresponded to C_1, and the C_2 was assigned to the arc in low frequency. According to Table 1, the values of C_1 and C_2 are both greater than 10^{-1} F cm^{-2}, thus the R_1 and R_2 are both indexed to the mass transfer process, involving gas molecular diffusion, adsorption and dissociation process on the electrode surface [30–33]. The electrode polarization resistance (R_p) equaled to the sum of R_1 and R_2. It is well known that the R_p is referred to the electrode reaction process, which usually contained the mass transfer and charge transfer in electrode [26, 31, 34]. But in our case, the R_p was just originated from mass transfer according to the value of characteristic capacitance. As shown in Table 1, R_p initially decreases first and then increases with the increase of the cell preparation pressure, and reached a minimum value at 10 MPa. It can be found that the minimal R_0 and R_p for 10 MPa cell bring about the best cell performance.

3.3 XRD analysis

Figure 3 presents the XRD comparison between the LCP, NCAL and LCP–NCAL SIM. From the XRD pattern of LCP, it can be found that the crystal structure of LCP is assigned to the fluorite phase with cubic structure, and no diffraction peaks with regard to La_2O_3 and Pr_2O_3 was detected [35]. Compared with standard card of CeO_2 (JCPDS no. 34-0394), the diffraction peak position of LCP slightly shifts to smaller angle. The ionic radius of dopant La^{3+} (1.16 Å) and Pr^{3+} (1.13 Å) is bigger than the Ce^{4+} (0.97 Å) counterpart; thus the La^{3+} and Pr^{3+} doping would expand the crystal lattice and lead to the shift toward lower angle [36]. The patterns of NCAL show sharp diffraction peaks, reflecting the good crystallinity of NCAL particles. For the LCP–NCAL SIMs,
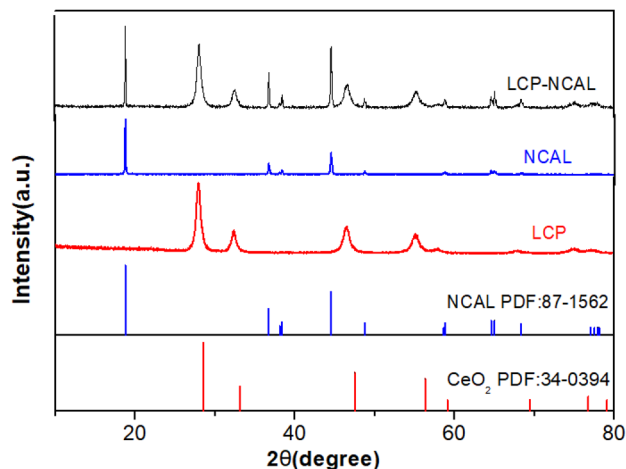

Fig. 3 XRD patterns of LCP, NCAL, and LCP–NCAL SIM

all diffraction peaks can be identified as the NCAL and LCP phase, no additional peaks discovered, indicating no chemical reaction was happened between LCP and NCAL two-phase materials. In addition, we have calculated the crystallite size of LCP particles and NCAL particles from the XRD patterns using the following Scherrer equation:

$$D = \frac{K\lambda}{\beta\cos\theta}$$

where D is the crystallite size, β is the full width at half-maximum height (FWHM), and θ is the Bragg diffraction angle. λ is the wavelength of the X-ray radiation (Cu $K\alpha = 0.15$ nm), and K is the Scherrer constant (0.89) [37–40]. The crystallite size of LCP (pure) and NCAL (pure) particles was calculated to be 11.80 nm and 44.37 nm, respectively. While for the LCP–NCAL SIM, the LCP (12.60 nm) and NCAL (38.80 nm) particles maintain almost the same size as the pure samples with some error.

3.4 SEM analysis

To obtain insight into the physical properties of commercial NCAL, the microstructure and composition of NCAL have been characterized. Figure 4a distinctly exhibits the detailed micrograph of commercial NCAL (pure). It can be
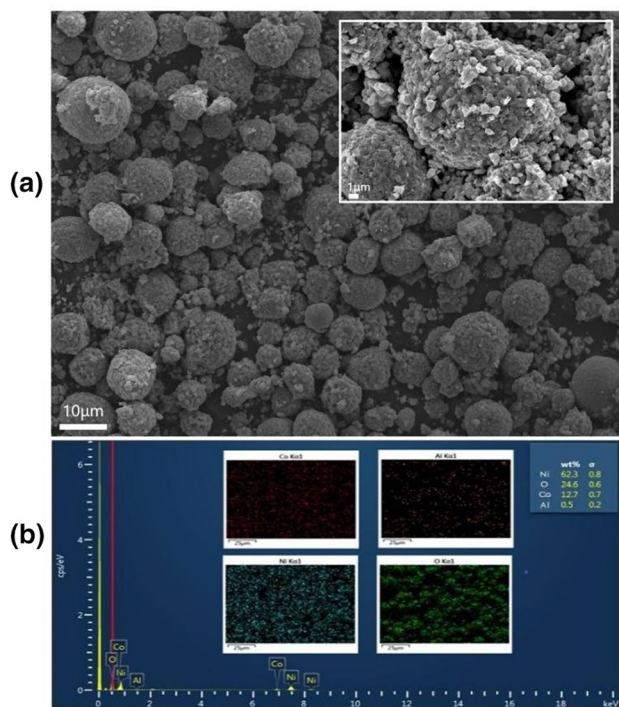
Fig. 4 a SEM micrograph of the commercial NCAL and **b** EDS and elemental mapping of the commercial NCAL

observed that lots of small nanosized particles agglomerated together to form big NCAL sphere, and the diameter of NCAL sphere is approximately 7–15 µm; the result is well agreed with our previous report [41]. Figure 4b gives EDS and elemental mapping of the commercial NCAL; the presence of Co, Al, Ni and O elements confirmed the main component of CoAlNi oxide, while the Li element has not been detected due to its low relative molecular mass. In addition, the surface area and pore volume of commercial NCAL were measured by Brunauer–Emmett–Teller (BET)

and Barrett–Joyner–Halenda (BJH) analysis using a nitrogen adsorption–desorption apparatus. The tested results revealed that the surface area of commercial NCAL was $0.3991 \, m^2 \, g^{-1}$ and the pore volume was 19.964 nm.

Figure 5a shows the cross-sectional view of the LCP–NCAL SIMFC pressed under 6 MPa loading. Three-layer configuration can be clearly observed. Among them, the two Ni–NCAL layers displayed almost the same thickness approximately 375 mµ, and the thickness of LCP–NCAL electrolyte membrane is about 700 mµ. Moreover, no obvious lamination and cracks were detected in the cross-sectional cell, indicating the small pressure of 6 MPa can also mold the cell configuration. Figure 5b exhibited the detailed morphology of LCP–NCAL membrane, and some big spheres can be observed in the membrane as the red circle marked, which should be NCAL phase. Previous report [41] and Fig. 4a show that, the morphological feature of NCAL is micron scale spherical particles. Thus, NCAL powders maintained the original morphology in the electrolyte membrane after pressing treatment. The nanosized particles of LCP could not be detected clearly due to the limitation of the instruments and equipment.

For determining the effect of preparation pressure on the electrolyte microstructure, we measured the interval between two NCAL spheres in electrolyte membrane to indirectly judge the density of LCP–NCAL membrane. Figure 6 shows the detailed morphology of electrolyte membrane pressed under different pressures: (a) 6 MPa, (b) 8 MPa, (c) 10 MPa, (d) 12 MPa. The intervals between NCAL spheres in electrolyte membrane were measured to be 6–8 µm, 4–6 µm, 3.5–4 µm, and 1–1.2 µm, respectively, corresponding to 6 MPa, 8 MPa, 10 MPa, and 12 MPa samples. Obviously, the interval gradually decreased with the increase of preparation pressure, and we can deduce that the density of the LCP–NCAL membrane gradually enhanced with the cell preparation pressure increasing. To get more
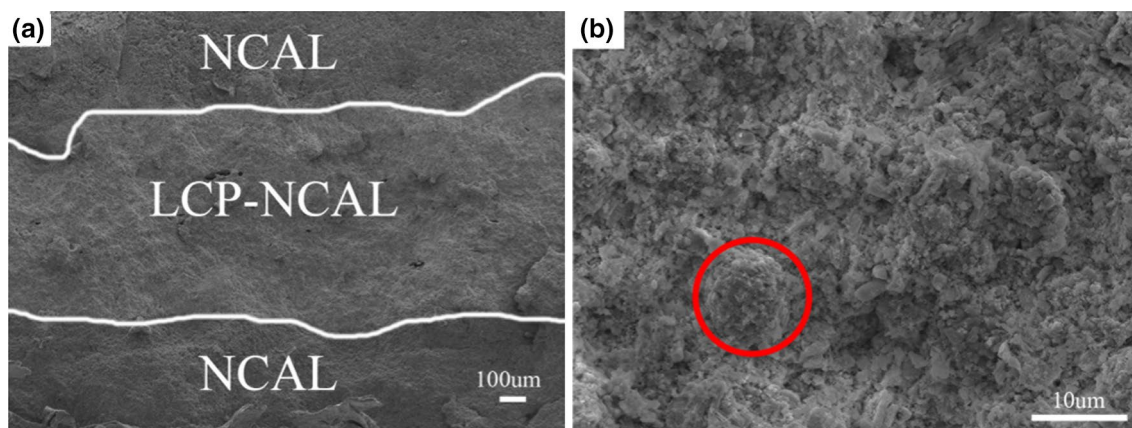

Fig. 5 a Cross-sectional SEM image of the cell pressed under 6 MPa loading and **b** the detailed morphology of LCP–NCAL electrolyte membrane
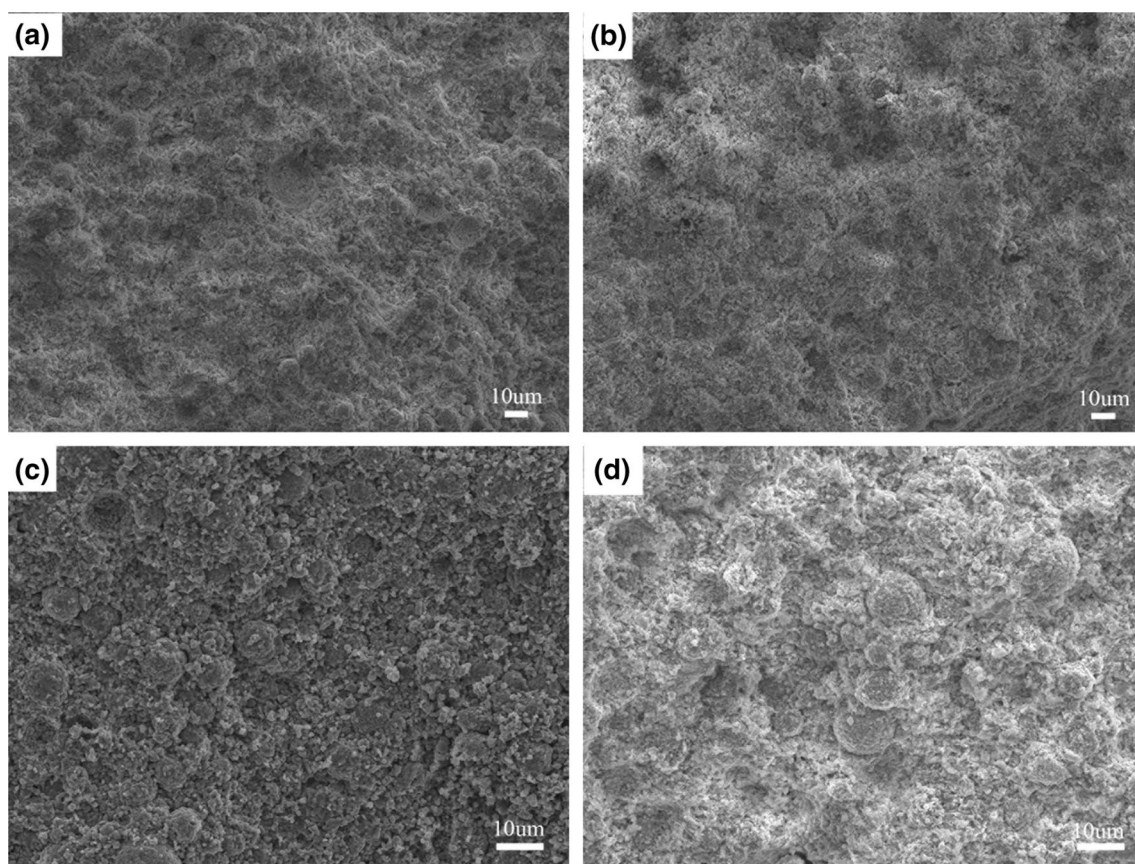
Fig. 6 Morphological comparison of LCP–NCAL membrane pressed under different pressures: **a** 6 MPa, **b** 8 MPa, **c** 10 MPa, **d** 12 MPa

detailed information, the porosity of SIM has been quantitatively analyzed by Archimedes method. According to the standard XRD cards, the ideal density (D) of LCP and NCAL is 7.2150 and 4.8480 g cm^{-3}, respectively. Thus, the LCP–NCAL SIM with 1:1 weight ratio has the ideal density of 6.0315 g cm^{-3}. Through Archimedes method, the actual density (D_T) of SIM is tested to be 3.9990 g cm^{-3} for 6 MPa pellet and 5.9380 g cm^{-3} for 10 MPa sample. Furthermore, the porosity (P) is calculated by the formula of $P = 1 - \frac{D_T}{D}$ to be 33.68% and 1.55% for the 6 MPa and 10 MPa samples, respectively. Obviously, the preparation pressure has a great impact on the porosity (P) of SIM, and the higher pressure brings about denser and lower porosity for the SIM.

Through the same method, we can also compare the microstructure of electrode pressed under different loadings. Figure 7 presents the morphological revolution of electrode layers with preparation pressure. For the four cells, the space between two NCAL spherical particles in electrode was determined to be 6–7.2 μm, 4–5.4 μm, 3.5–4 μm and 0.9–1.3 μm, respectively. Therefore, the NCAL sphere space in electrode layer gradually decrease with the increase of preparation pressure; thus it can be speculated that the porosity of electrode deteriorated with preparation pressure.

Figure 8a shows the typical I–V and I–P curves of SOFC pressed under 6 MPa at different hydrogen flow rates. When the hydrogen flow rate was 75 ml min^{-1}, the OCV and P_{max}, respectively, delivered low value of 0.4 V and 57 mW cm^{-2} at 550 °C. As the hydrogen flow rate increases, the OCV and the P_{max} of the cell gradually enhanced; this can be attributed to the improvement of hydrogen partial pressure. While the hydrogen was supplied at 150 ml min^{-1}, an OCV of 1.01 V and a P_{max} of 1154 mW cm^{-2} were received. But as the hydrogen flow rate continually increased, the OCV changed slightly and the P_{max} decreased. Since the hydrogen flow rate reached 200 ml min^{-1}, the P_{max} decreased to 600 mW cm^{-2}. Therefore, we can conclude that the optimal hydrogen flow rate for 6 MPa SIMFC was 150 ml min^{-1}. Figure 8b gives electrochemical performance of SIMFC pressed under 10 MPa at different hydrogen flow rates. Similarly, when the hydrogen flow rate was 75 ml min^{-1}, the OCV displayed a low value of 0.74 V, and the P_{max} was just 280 mW cm^{-2}. It can be seen that the OCV and the P_{max} of these cells increase with the hydrogen flow rate due to the enhancement of hydrogen partial pressure. But when the hydrogen flow rate was 175 ml min^{-1}, the cell performance reached an optimum status, i.e., the OCV of 0.98 V and the
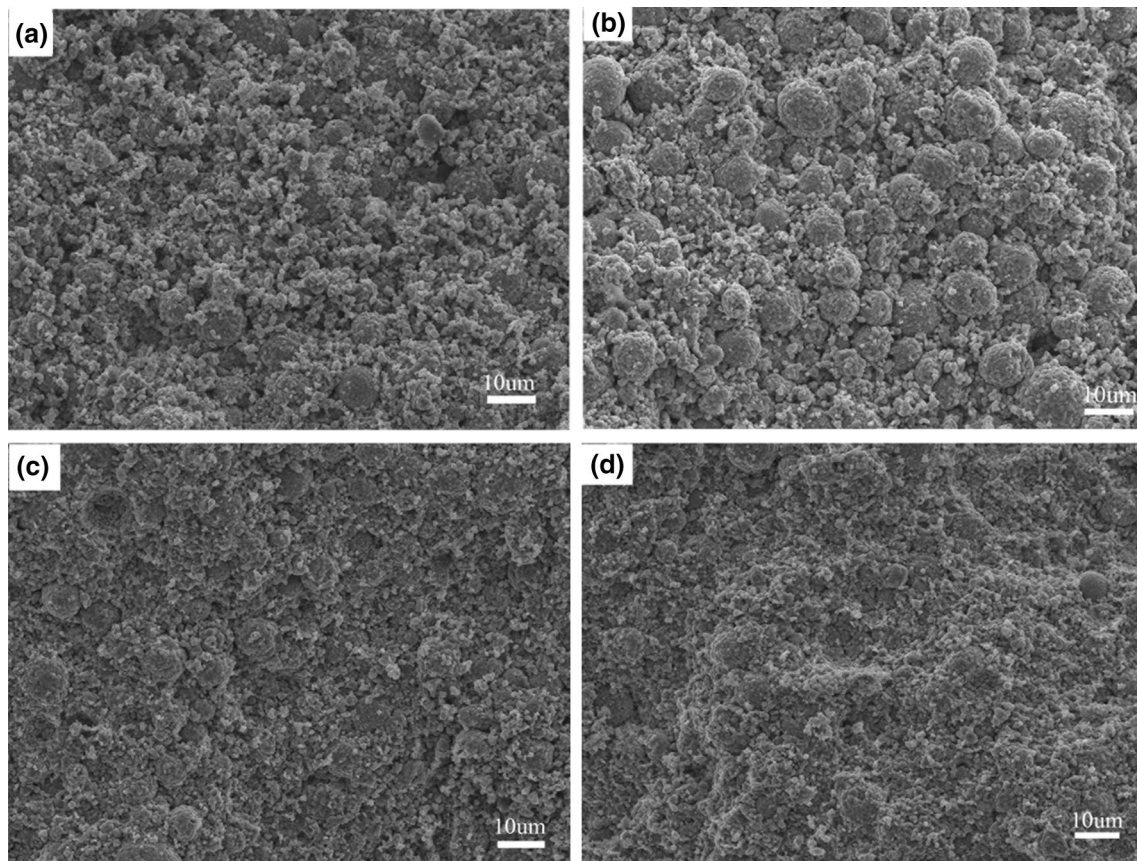
Fig. 7 Detailed morphology of the Ni–NCAL electrode pressed under different pressures: **a** 6 MPa, **b** 8 MPa, **c** 10 MPa, **d** 12 MPa
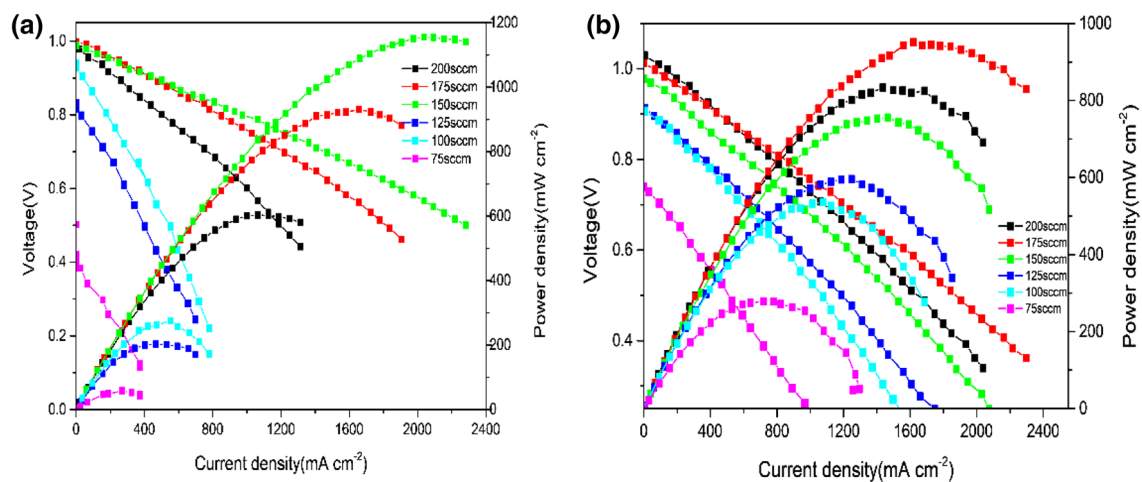

Fig. 8 Electrochemical performance of cell obtained under 6 MPa (**a**) and 10 MPa (**b**) pressure as the hydrogen flow rate changed from 75 to 200 ml min^{-1}

P_{max} of 950 mW cm^{-2}. When the hydrogen flow rate was further increased to 200 ml min^{-1}, the OCV remained almost unchanged but the P_{max} was deteriorated to 833 mW cm^{-2}. Thus, the optimal hydrogen flow rate of 10 MPa SIMFC was

175 ml min^{-1}. Compared Fig. 7a with b, it can be found that the change trend of cell performance with hydrogen flow rate is extremely similar, but the optimal hydrogen flow rate was different for samples pressed under various loadings.

During the performance testing procedure, the hydrogen partial pressure on anode side increases with hydrogen flow rate; more hydrogen can be oxidized and the mass transport was also enhanced with the increase of gas mobility; all the factors resulted in the improvement of cell performance with hydrogen flow rate. However, while hydrogen was supplied at high flow rate, the hydrogen can penetrate the cell interior to contact with oxygen; this should bring about shorting circuit problem to decrease the cell performance. As the SEM image and porosity analysis presented, the electrolyte membrane pressed at 10 MPa has better density than that of 6 MPa; thus the 10 MPa SIMFC have more excellent stability compared with 6 MPa cell.

4 Conclusion

A series of LCP–NCAL SIMFCs has been fabricated under different loadings. The microstructure, the electrochemical performance and the electrochemical impedance of cells were systematically characterized to detect the influence of preparation pressure. As the experimental results revealed, when the cell preparation pressure increases from 6 to 10 MPa, the peak power density increases from 449 to 811 mW cm^{-2} at 550 °C, and the OCV changes slightly. But while the cell preparation continually increased to 12 MPa, the peak power density decreased to 446 mW cm^{-2}. The optimal cell performance was received at 10 MPa loading. As the SEM image and porosity analysis exhibited, the high preparation pressure resulted in the excellent density of the electrolyte layer to promote the cell performance, and it also damage the porous structure of the electrode to further reduce the electrochemical performance. On the other hand, although the low preparation pressure can ensure the porosity of the electrode to enhance cell performance, simultaneously the electrolyte also maintained porous to further deteriorate the cell performance under low preparation pressure. Therefore, 10 MPa pressure results in the supreme cell microstructure and further give rise to the optimal cell performance.

References

1. W.W. Zhong, W.G. Tu, S.S. Feng, A.J. Xu, J. Alloys Compd. **772**, 669–674 (2019)
2. W.W. Zhong, S.J. Shen, S.S. Feng, Z.P. Lin, Z.P. Wang, B.Z. Fang, CrystEngComm **20**, 7749–7460 (2018)
3. B.C.H. Steele, A. Henizel, Nature **414**, 345–352 (2001)
4. S.C. Singhal, Solid State Ionics **152**, 405–410 (2002)
5. S. Mcintosh, R.J. Gorte, Chem. Rev. **104**, 4845–4865 (2004)
6. S. Mcintosh, Annu. Rev. Chem. Biomol. Eng. **2**, 9–30 (2011)
7. R.M. Ormerod, Chem. Soc. Rev. **32**(1), 17–28 (2003)
8. I. Khan, P.K. Tiwari, S. Basu, Electrochim. Acta **294**, 1–10 (2019)
9. B.C.H. Steel, A. Heinzel, Nature **414**(6861), 345–352 (2001)
10. S.C. Singhal, Solid State Ionics **135**, 305–313 (2000)
11. E.D. Wachsmam, K.T. Lee, Science **334**, 935–939 (2011)
12. H. Deng, C. Feng, W. Zhang, Y.Q. Mi, X.Y. Wang, W.J. Dong, B.Y. Wang, B. Zhu, Int. J. Hydrogen Energy **42**, 25001–25007 (2017)
13. C. Xia, Z. Qiao, C. Feng, C. Feng, J.S. Kim, B.Y. Wang, B. Zhu, Materials **11**(1), 40 (2018)
14. B. Zhu, L.D. Fan, H. Deng, Y.J. He, M. Afzal, W.J. Dong, A. Yaqub, N.K. Janjua, J. Power Sources **316**, 37–43 (2016)
15. M. Koyama, C.J. Wen, T. Masuyanma, J. Otomo, H. Fukunaga, K. Yamada, K. Eguchi, H. Takahashi, J. Electrochem. Soc. **148**(7), 795–801 (2001)
16. H. Dai, H. Chen, S. He, G. Cai, L. Guo, J. Power Sources **286**, 427–430 (2015)
17. S. Lee, E.S. Oh, J. Power Sources **244**, 721–725 (2013)
18. B. Zhu, J. Nanosci. Nanotechnol. **11**, 8873–8879 (2011)
19. B. Zhu, World J. Eng. **2**, 2 (1970)
20. J. Zhu, H. Deng, B. Zhu, W.J. Dong, W. Zhang, J.J. Li, X.J. Bao, Ceram. Int. **43**, 5484–5489 (2017)
21. X.T. Zhu, J. Yang, D. Dastan, H. Garmestani, R.H. Fan, Z.H. Shi, Compos. A **125**, 105521 (2019)
22. X.T. Yin, D. Dastan, F.Y. W, J. Li, Nanomaterials. **9**, 1163 (2019).
23. D. Dastan, A. Banpurkar, J. Mater. Sci. Mater. Electron. **28**(4), 3851–3859 (2016)
24. D. Dastan, S.W. Gosavi, N.B. Chaure, Macromol. Symp. **347**, 81–86 (2015)
25. X.T. Yin, W.D. Zhou, J. Li, Q. Wang, F.Y. Wu, D. Dastan, D. Wang, H. Garmestani, X.M. Wang, Ştefan Ţălu. J. Alloys Compd. **805**, 229–236 (2019)
26. L.D. Fan, H.J. Zhang, M.M. Chen, C.Y. Wang, H. Wang, M. Singh, B. Zhu, J. Hydrogen Energy **38**, 11398–11405 (2013)
27. X.Y. Nie, Y. Chen, N. Mushtaq, S. Rauf, B.Y. Wang, W.J. Dong, X.Y. Wang, H. Wang, B. Zhu, Nanoscale Res. Lett. **14**, 162 (2019)
28. C. Xia, Y.X. Cai, B.Y. Wang, M. Afzal, W. Zhang, A. Soltaninazarlou, B. Zhu, J. Power Sources **342**, 779–786 (2017)
29. H.Q. Hu, Q.Z. Lin, A. Muhammd, B. Zhu, J. Power Sources **286**, 388–393 (2015)
30. L.D. Fan, P.C. Su, J. Power Sources **306**, 369–377 (2016)
31. S.B. Adler, Chem. Rev. **104**, 4791–4843 (2004)
32. E. Perry Murray, M.J. Sever, S.A. Barnett, Solid State Ionics **148**, 27–34 (2002)
33. Y. Li, R. Gemmen, X. Liu, J. Power Sources **195**, 3345–3358 (2010)
34. S.B. Adler, X.Y. Chen, J.R. Wilson, J. Catal. **245**, 91–109 (2007)
35. C. Xia, B.Y. Wang, Y.X. Cai, W. Zhang, M. Afzal, B. Zhu, Electrochem. Commun. **77**, 44–48 (2017)
36. B.C.H. Steele, Solid State Ionics **129**, 95–110 (2000)
37. D. Dastan, Appl. Phys. A **123**(699), 1–13 (2017)
38. D. Dastan, J. Atomic, Mol. Condens. Nano Phys. (JAMCNP) **2**(2), 109–114 (2015)
39. A. Jafari, M.H. Alam, D. Dastan, S. Ziakhodadadian, Z.C. Shi, H. Garmestani, A.S. Weidenbach, Ştefan Ţălu. J. Mater. Sci. Mater. Electron. **30**, 21185–21198 (2019)
40. D. Dastan, N. Chaure, M. Kartha, J. Mater. Sci. Mater. Electron. **28**, 7784–7796 (2017)
41. X.Q. Liu, W.J. Dong, Y.Z. Tong, L.L. Wei, M.H. Yuan, X.Y. Wang, B.Y. Wang, B. Zhu, Electrochim. Acta **295**, 325–332 (2019)